Supplementary Information (Supplementary Figures and Tables)

E22G Aβ40 fibril structure and kinetics illuminate how Aβ40 rather than Aβ42 triggers familial Alzheimer's

Mohammad Jafar Tehrani[a], Isamu Matsuda[a], Atsushi Yamagata[b], Yu Kodama[a], Tatsuya Matsunaga[a, b], Mayuko Sato[c], Kiminori Toyooka[c], Dan McElheny,[d] Naohiro Kobayashi[b], Mikako Shirouzu[b], Yoshitaka Ishii[a, b, *]

[a] *School of Life Science and Technology, Tokyo Institute of Technology, 4259 Nagatsuta-cho, Midori-ku, Yokohama, Kanagawa 226-8503, Japan*

[b] *RIKEN Center for Biosystems Dynamics Research, 1-7-22 Suehiro-cho, Tsurumi-ku, Yokohama, Kanagawa 230-0045, Japan*

[c] *RIKEN Center for Sustainable Resource Science, 1-7-22 Suehiro-cho, Tsurumi-ku, Yokohama, Kanagawa 230-0045, Japan*

[d] *Department of Chemistry, University of Illinois at Chicago, 845 W Taylor St, Chicago, IL 60607, USA*

Supplementary Figures

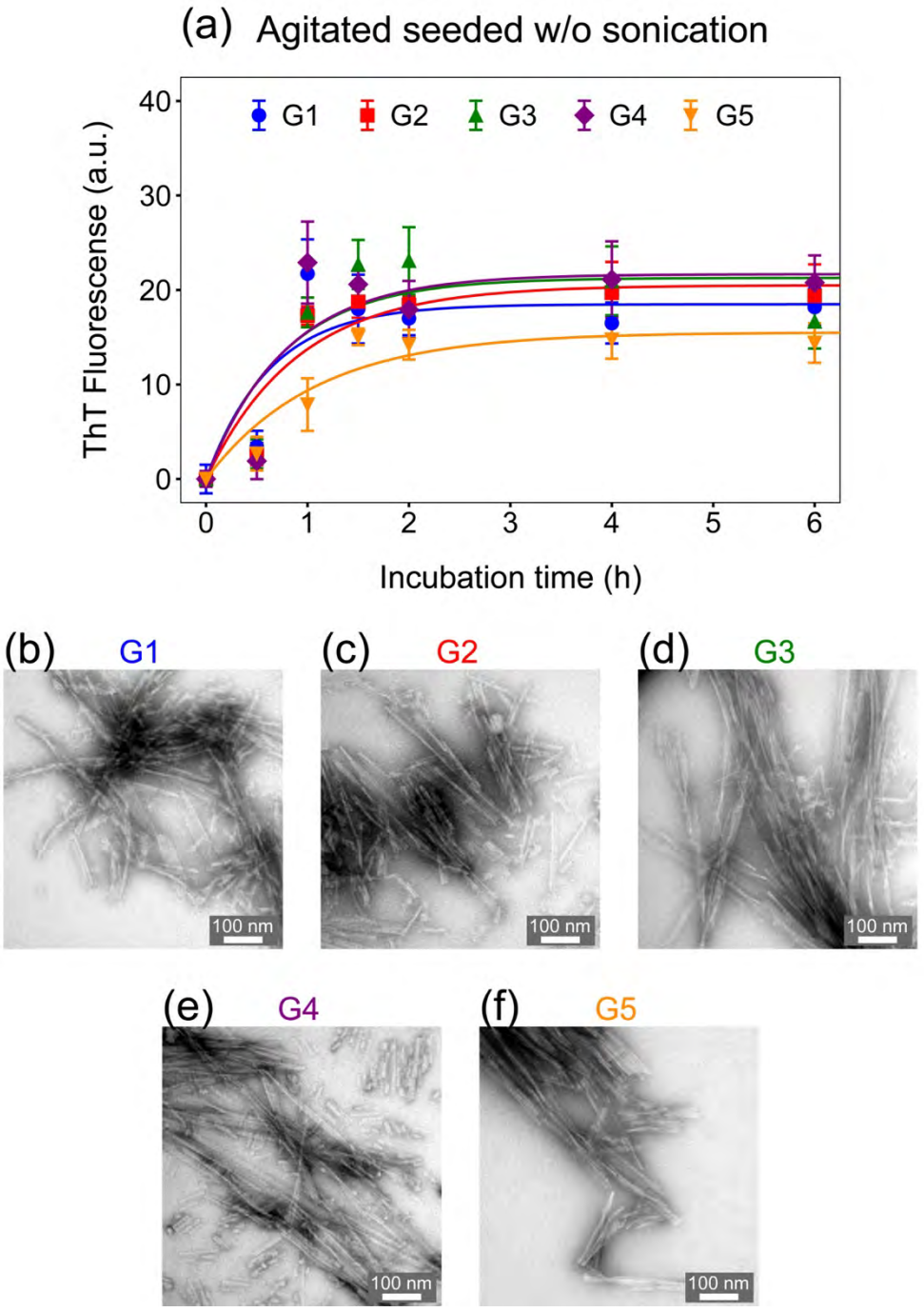

Supplementary Figure 1. (a) Kinetics of seeded aggregation of E22G Aβ40 under agitated incubation, seeded with unfragmented mature E22G Aβ40 fibrils as seeds, where the seeds were not sonicated. ThT fluorescence intensity is shown in arbitrary unit (a.u.). Each data point represents the average of independently measured fluorescence values ($N = 3$) after subtracting the baseline, which was estimated from the average fluorescence value at the first time point. The error bars were estimated from the standard deviation as described for Fig. 1(k, l). (b–f) corresponding TEM images for G1 to G5 fibrils, respectively. The analysis of the kinetic data was performed as described for Fig. 1.

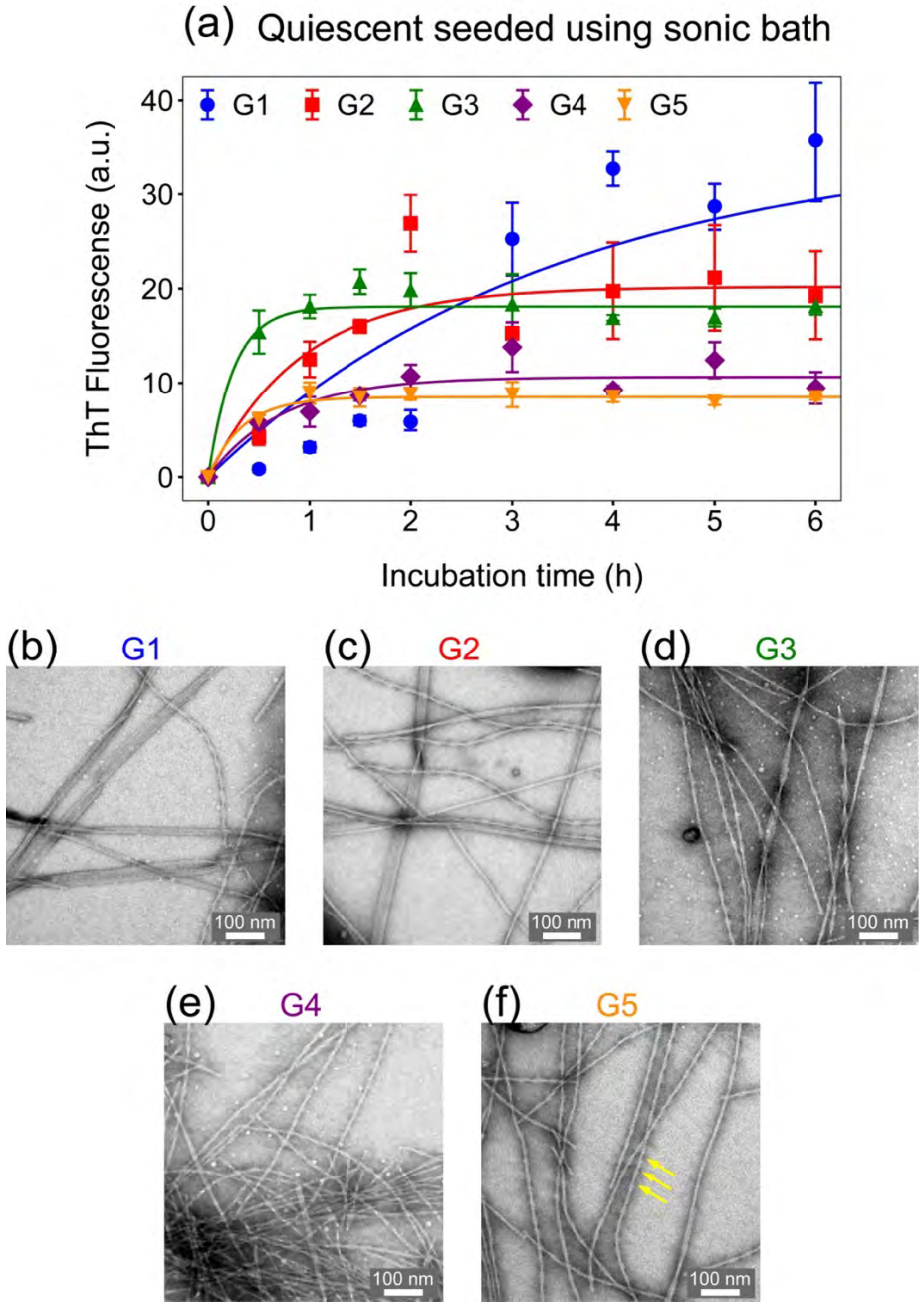

Supplementary Figure 2. (a) Incubation-time dependence of ThT fluorescence for E22G Aβ40 under quiescent incubation, seeded with fragmented mature E22G Aβ40 fibrils as seeds, where the seeds were sonicated by sonic bath. ThT fluorescence intensity is shown in arbitrary unit (a.u.). Each data point represents the average of independently measured fluorescence values (N = 3) after subtracting the baseline, which was estimated from the average fluorescence value at the first time point. The error bars were estimated from the standard deviation as described for Fig. 1(k, l). (b–f) corresponding TEM images for G1 to G5 fibrils, respectively. The yellow arrows in (f) indicate the approximate cross-over locations. The cross-over distance showed similar 35–45 nm periodicities in the dominant twisted morphology, compared with the quiescent E22G Aβ40 fibrils seeded with E22G Aβ40 fibrils fragmented by homogenizer. The analysis of the kinetic data was performed as described for Fig. 1.

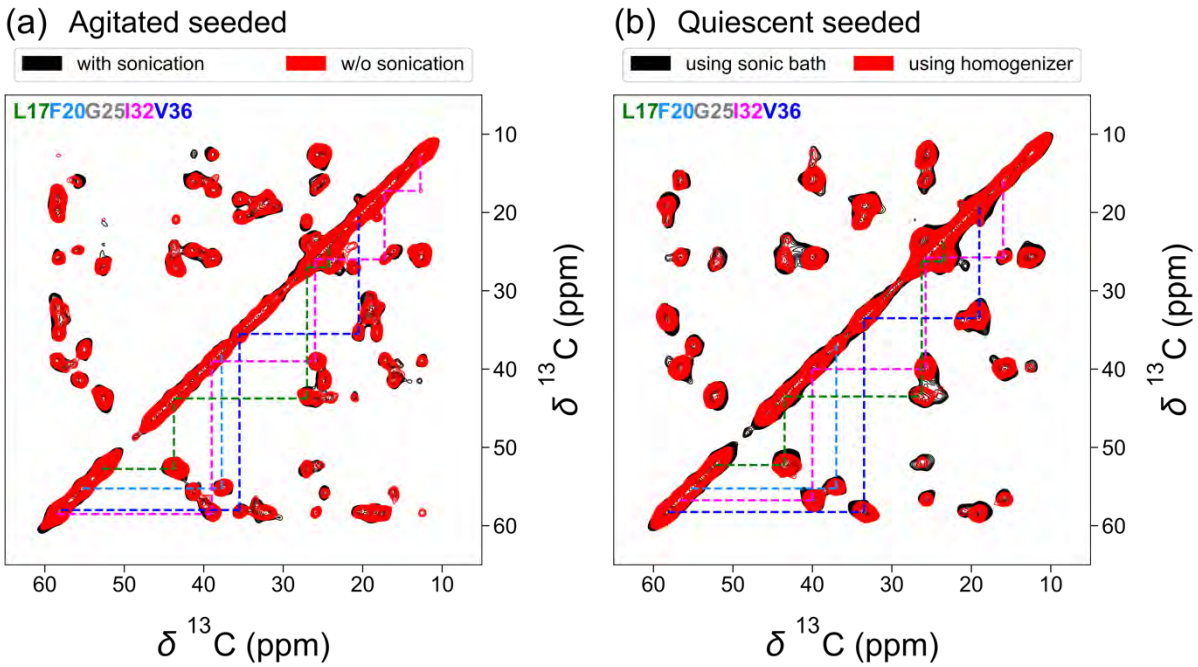

Supplementary Figure 3. 2D ^{13}C-^{13}C correlation SSNMR spectra of seeded E22G Aβ40 fibrils uniformly ^{13}C- and ^{15}N-labeled at L17, F20, G25, I32, and V36. (a) Agitated E22G Aβ40 fibrils seeded with fragmented E22G Aβ40 fibrils, where the seeds were sonicated by a sonic bath in black, and with unfragmented E22G Aβ40 fibrils in red. (b) Quiescent E22G Aβ40 fibrils seeded with fragmented E22G Aβ40 fibrils, where the seeds were sonicated by homogenizer in red, and sonicated by sonic bath in black. Contour levels were adjusted to (a) 9%, and (b) 5% of the $^{13}C_{\alpha}$-$^{13}C_{\alpha}$ diagonal signal of G25. In (b), the line widths for the sample prepared with a sonic bath are generally broader. ^{13}C chemical shifts are designated by δ ^{13}C. Since the SSNMR spectra indicated more homogeneous conformation for the quiescent E22G Aβ40 fibril sample using seeds prepared with homogenizer, we adopted the protocol.

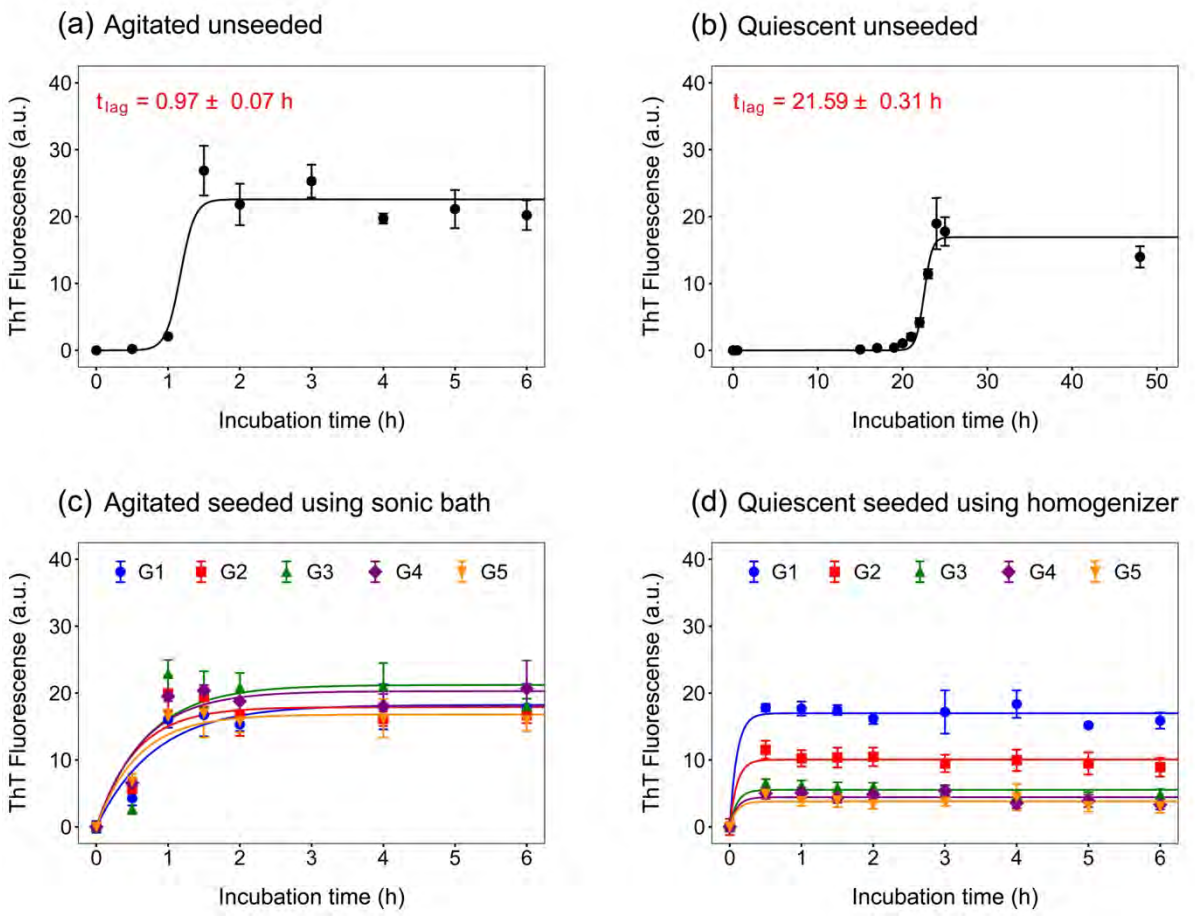

Supplementary Figure 4. Incubation-time dependence of ThT fluorescence of E22G Aβ40 monomers incubated at 37 ºC for (a) agitated G0 and (b) quiescent G0 with the lag time shown in the inset. Incubation-time dependence of ThT fluorescence (in arbitrary unit, a.u.) of E22G Aβ40 monomers incubated with fragmented E22G Aβ40 fibrils at 37ºC in the (c) agitated (seeds were fragmented by sonic bath) and (d) quiescent (seeds were fragmented by homogenizer) conditions. The decline in ThT fluorescence intensity is observed in (d) in higher generations (G2–G5). The analysis of the kinetic data was performed as described for Fig. 1. All the data points in the graphs display the average of independently measured fluorescence values (N = 3) after subtracting the baseline, which was estimated from the average fluorescence value at the first time point. The error bars were estimated from the standard deviation as described for Fig. 1(k, l).

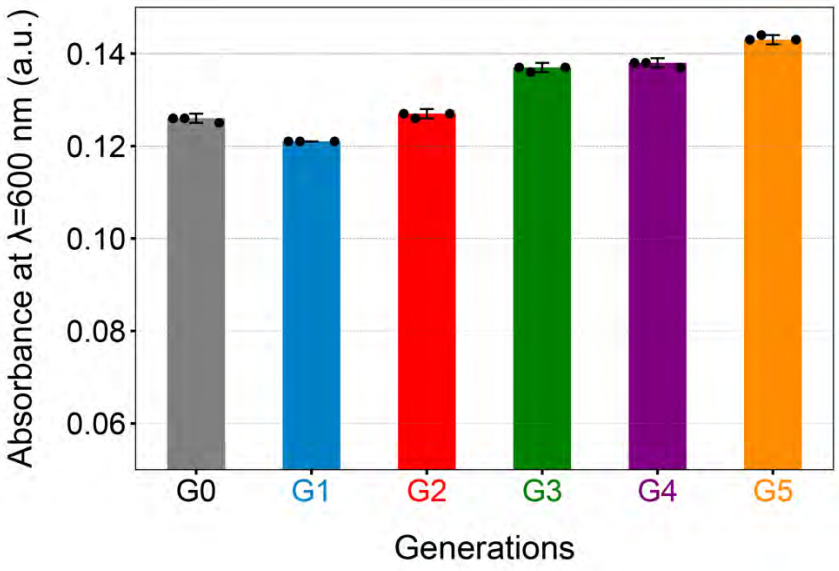

Supplementary Figure 5. Turbidity of quiescent E22G Aβ40 fibril samples for different generations from unseeded (G0) to seeded (G1–G5) measured at λ=600 nm. Seeds used for the preparation of G1 to G5 were fragmented by homogenizer. The absorbance value was obtained for each data as the average for three separate measurements (N = 3) in arbitrary unit (a.u.), with an error bar indicating the standard deviation. Data distributions for each generation are shown as dot plots on the corresponding bar.

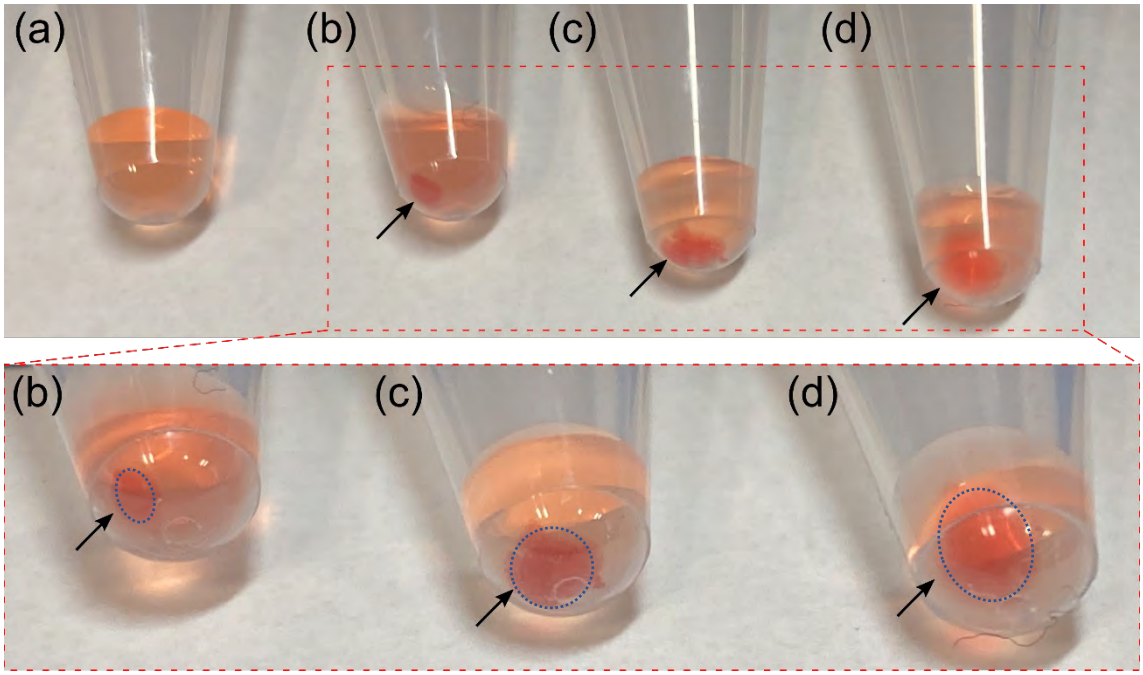

Supplementary Figure 6. A picture of Congo-red stained precipitates (black arrows) of (b) agitated WT Aβ40 fibril, (c) agitated G5 E22G Aβ40 fibril, and (d) quiescent G4 E22G Aβ40 fibril samples, which were obtained after centrifugating the solutions containing suspended Aβ fibrils at 4,000 g for 5 min. The sample (a) is a control for a phosphate buffer mixed with Congo red. The outlined area (dotted blue line) of the precipitate in (d) is approximately 5.4 and 1.6 times larger than those in (b) and (c), respectively. The samples (b–d) were prepared by incubating ~40 μM WT Aβ and ~25 μM E22G Aβ for 3–4 days. An aliquot of 45 μL of the resultant solutions was used for the assay and mixed with a 500 μM Congo-red solution of 5 μL. The volume ratio of the precipitates between (d) and (b) and that between (c) and (b) are 11.5 ± 5.3 and 7.5 ± 2.8, respectively. The volume of the precipitate was estimated by measuring the weight difference of the entire solution and the supernatant (N = 9, 3, 5 for (b), (c), (d), respectively; one outlier was removed from (b) by Q-test with 95% confidence interval). The densities of the solutions were assumed to be identical.

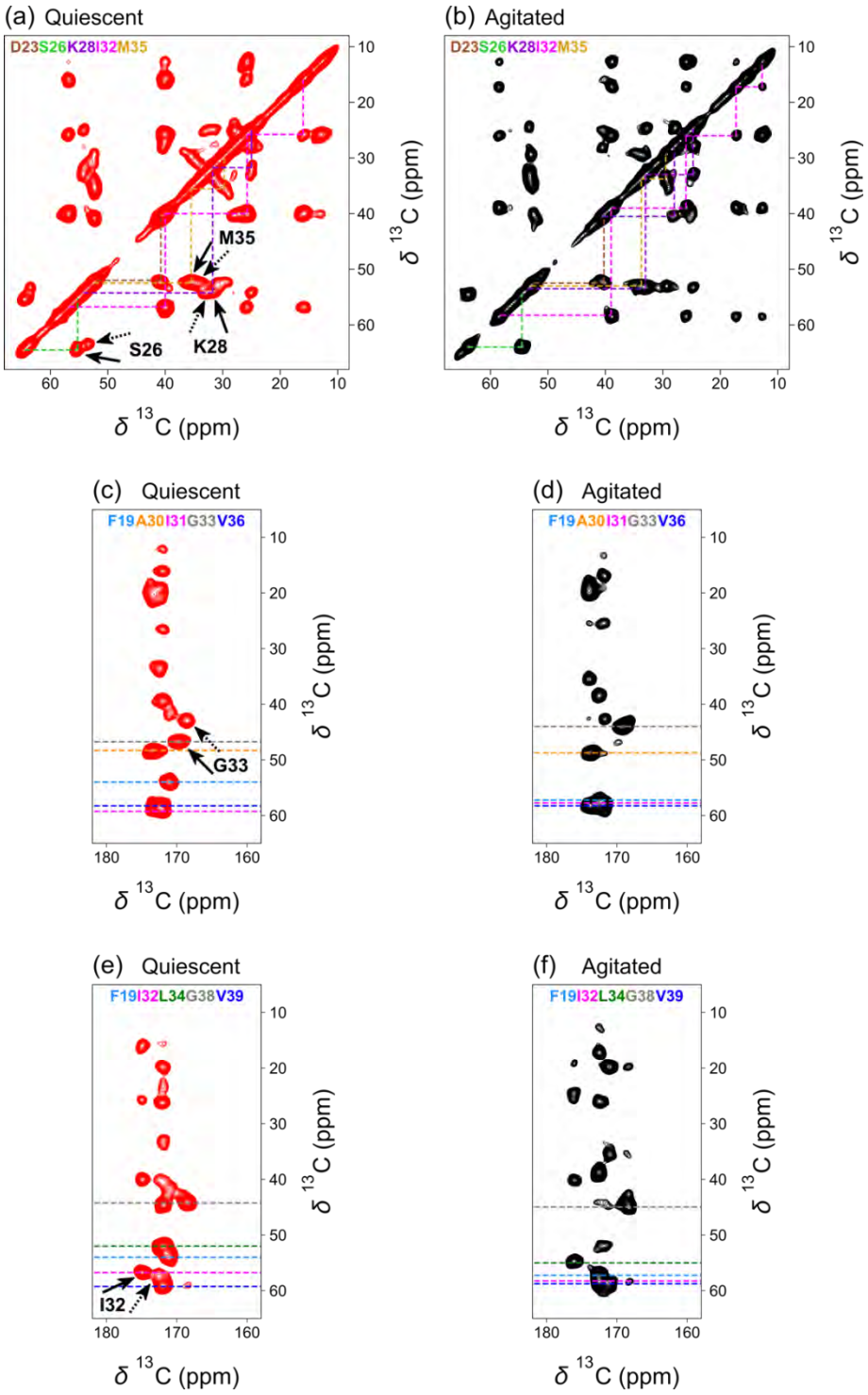

Supplementary Figure 7. 2D ^{13}C-^{13}C correlation SSNMR spectra of seeded E22G Aβ40 fibrils: agitated fibrils (seeds were fragmented by sonic bath) in black and quiescent fibrils (seeds were fragmented by homogenizer) in red. The samples were uniformly ^{13}C- and ^{15}N-labeled at (a, b) D23, S26, K28, I32, M35, (c, d) F19, A30, I31, G33, V36, and (e, f) F19, I32, L34, G38, and V39 residues. Contour levels were adjusted to (a, b) 4% of I32, (c, d) 5% of A30, and (e, f) 6% of L34 $^{13}C_\alpha$-$^{13}C_\alpha$ diagonal signals. Black solid and dotted arrows indicate major and minor signals, respectively, for the designated residues. ^{13}C chemical shifts are designated by δ ^{13}C.

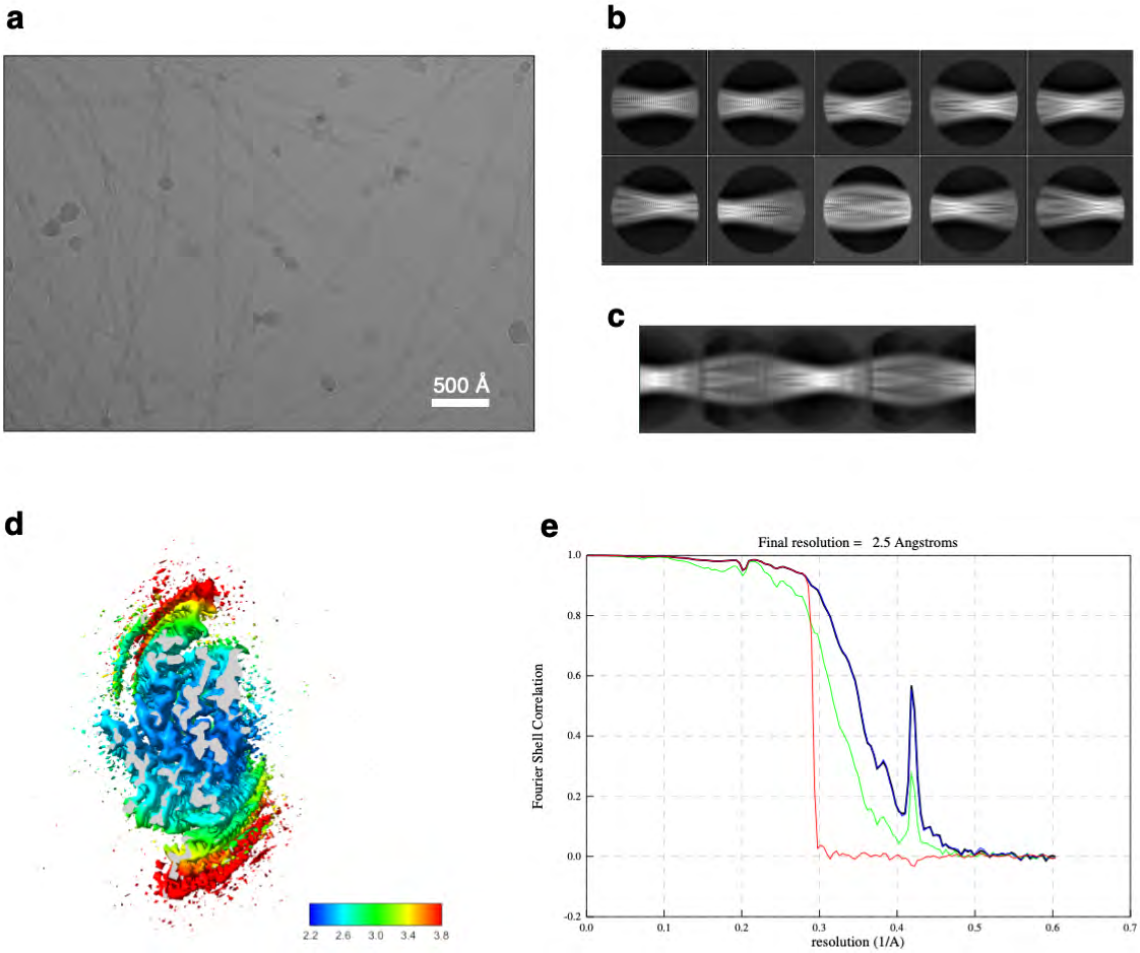

Supplementary Figure 8. (a) Representative cryoEM micrograph. (b) Representative 2D class averages. (c) Assembly of the multiple 2D class averages generated by relion_helix_inimodel2D of Relion-3.1. (d) Local resolution estimation for the map calculated by Relion LocalRes. (e) FSC curves between two half-maps (black line = FSC corrected, green line = FSC unmasked map, blue line = FSC masked map, red line = corrected FSC phase randomized masked map).

	*C*1	*C*2	*pseudoC2*$_1$
3D auto-refinement			
twist (°)	-2.17	-2.17	178.935
rise (Å)	4.766	4.766	2.383
imposed symmetry	*C*1	*C*2	*C*1
Estimated resolution (Å)	3.03	3.11	3.14

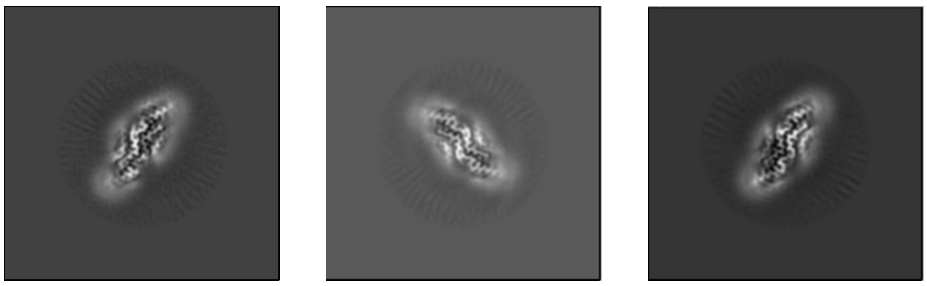

Postprocess			
Map resolution (Å)	2.86	2.86	2.89

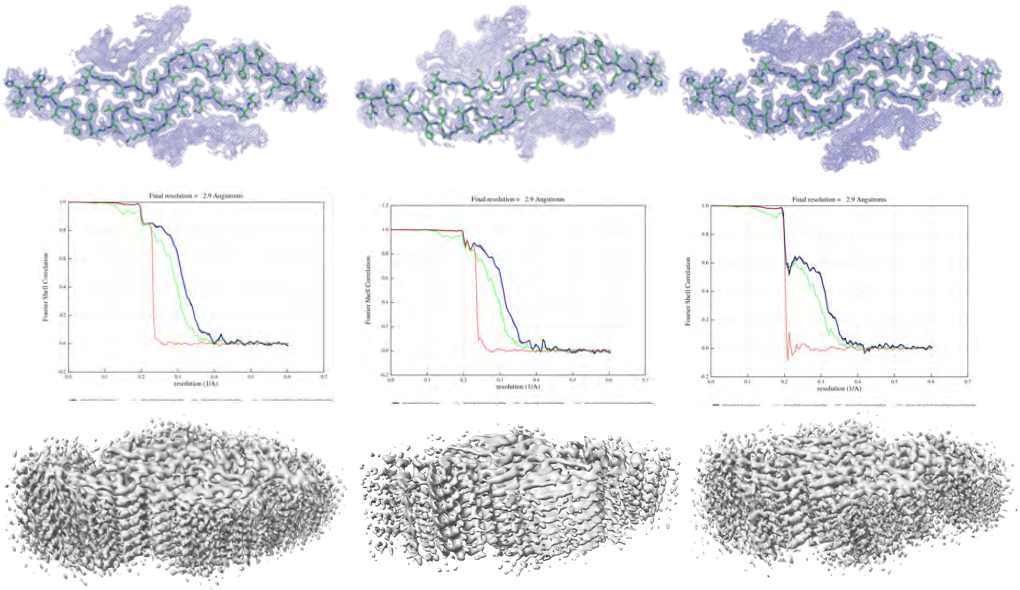

Supplementary Figure 9. The cryo-EM maps with C1, C2, and pseudo $C2_1$ symmetry. The cryo-EM maps were reconstructed by 3D auto-refinement and Postprocessing, with C1, an imposed C2, and pseudo-$C2_1$ symmetries, respectively.

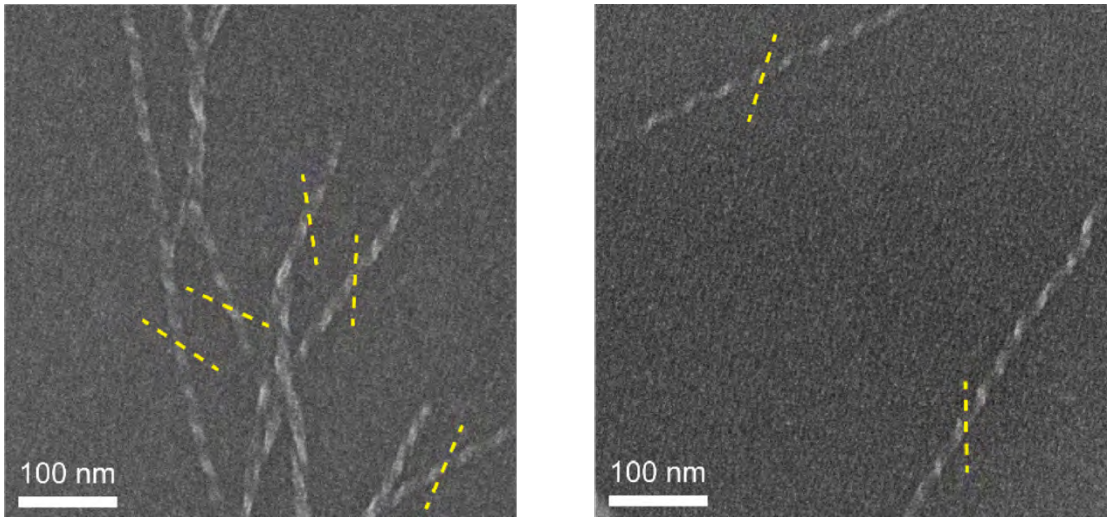

Supplementary Figure 10. SEM images of quiescent seeded E22G Aβ40 fibril obtained in two different regions of the grid. It contains left-handed twisted fibrils.

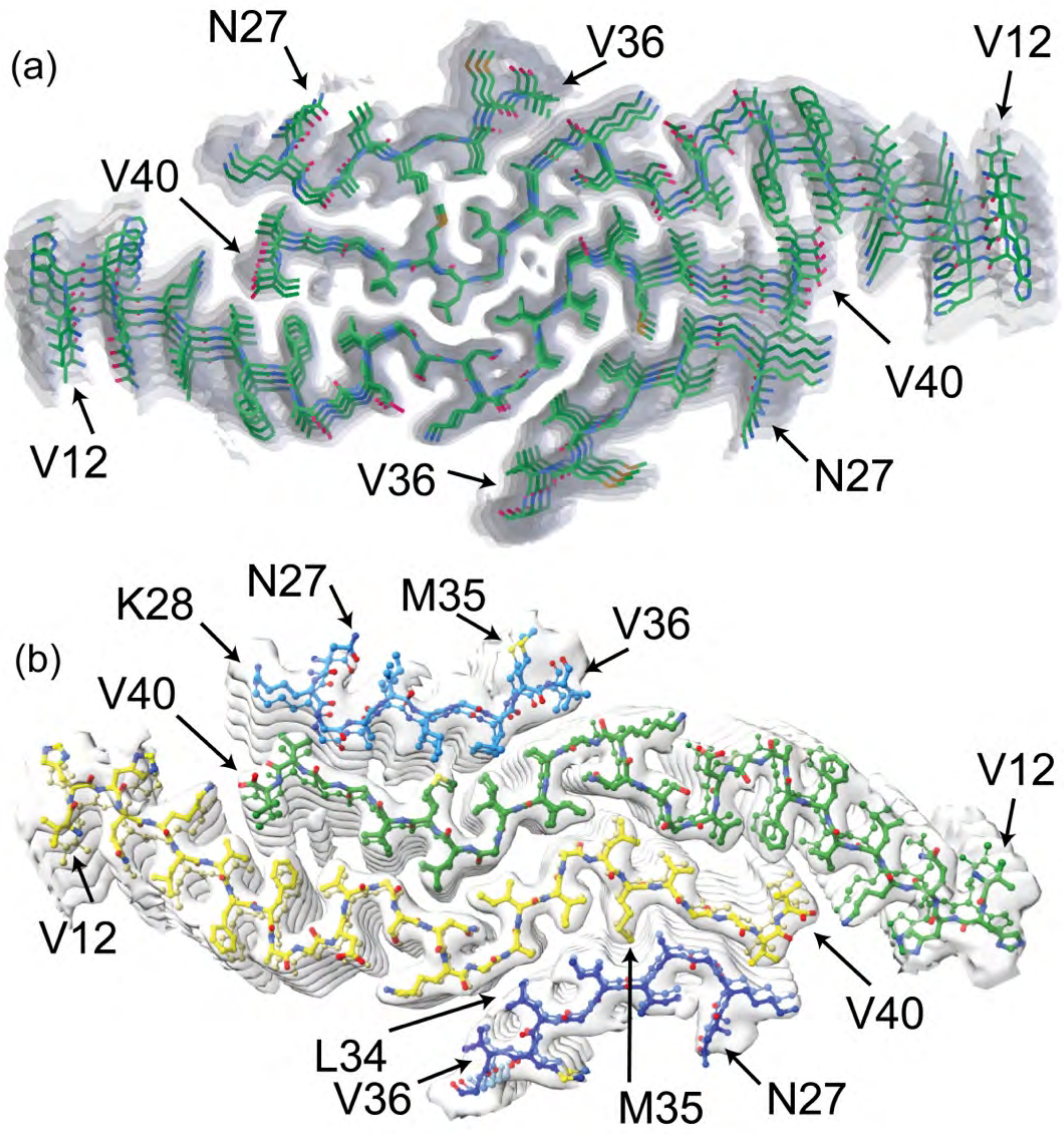

Supplementary Figure 11. CryoEM map obtained for the seeded quiescent E22G Aβ40 fibrils, overlaid with the tentative models of the outer two layers and two core layer structures. The models in (a) and (b) correspond to those for the core-layer models in Fig. 3(b) and (d), respectively.

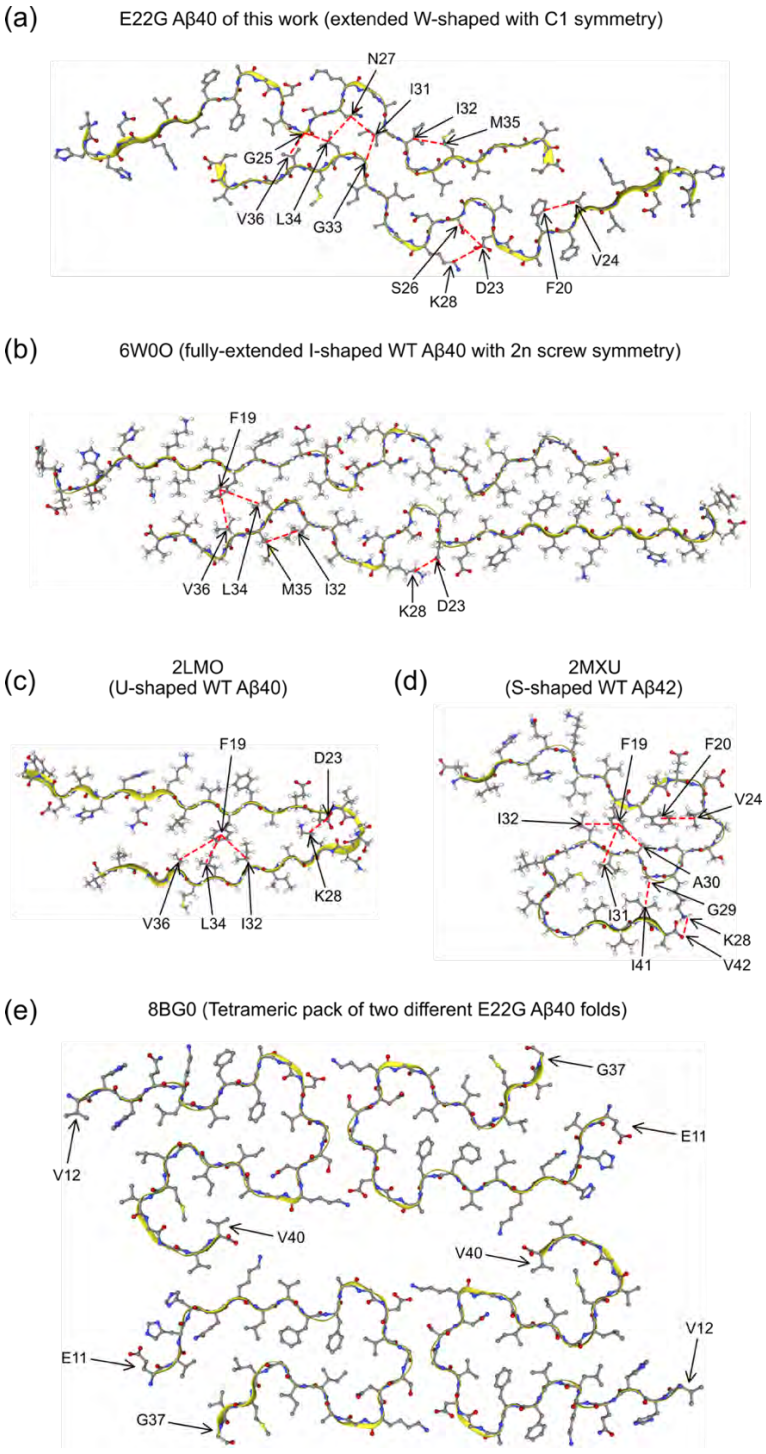

Supplementary Figure 12. Comparison of Aβ fibril structures from this work and other works with designated structural constraints obtained from SSNMR data in each work: (a) Structural model of E22G Aβ40 fibril proposed in this work. Previously published structural models of (b) brain-derived WT Aβ40 fibril reported by Ghosh *et al.* (6W0O)[1], (c) synthetic U-shaped WT Aβ40 fibril reported by Petkova *et al.* (2LMO)[2-4], and (d) synthetic S-shaped WT Aβ42 fibril reported by Xiao *et al.* (2MXU)[5], and (e) tetrameric form of two different folds of E22G Aβ from FAD human brain (8BG0)[6]. PDB identifiers are indicated with the labels in (b–e). The structures highlight those long-range structural constraints observed for the quiescent E22G Aβ40 fibril in (a) are different from those in the previous studies. Aβ fibrils were illustrated by Biopython[7] together with NGLview[8].

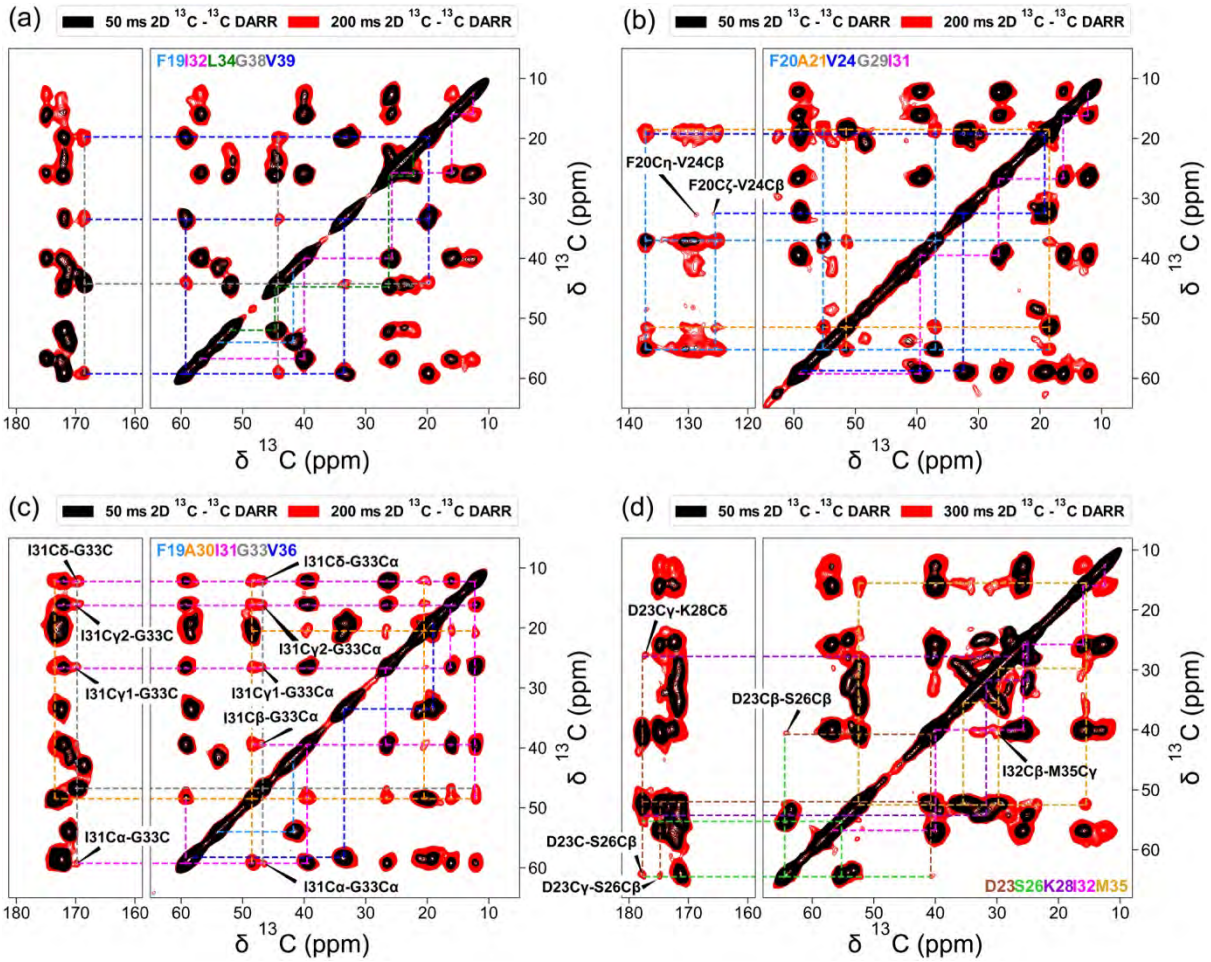

Supplementary Figure 13. Additional long-range 2D ^{13}C-^{13}C correlation SSNMR spectra for quiescent seeded E22G Aβ40 fibril samples uniformly ^{13}C-, ^{15}N-labeled at (a) F19, I32, L34, G38, V39, (b) F20, A21, V24, G29, I31, (c) F19, A30, I31, G33, V36, and (d) D23, S26, K28, I32, 35. The identified long-range ^{13}C-^{13}C contacts were (b) F20–V24, (c) I31–G33, and (d) D23–S26, D23–K28, and I32–M35, confirming the expected constraints in the model obtained by cryoEM. The base-contour levels are adjusted to 4–5 (in red) and 6–8 (in black) times the root-mean-squared noise level. ^{13}C chemical shifts are designated by δ ^{13}C.

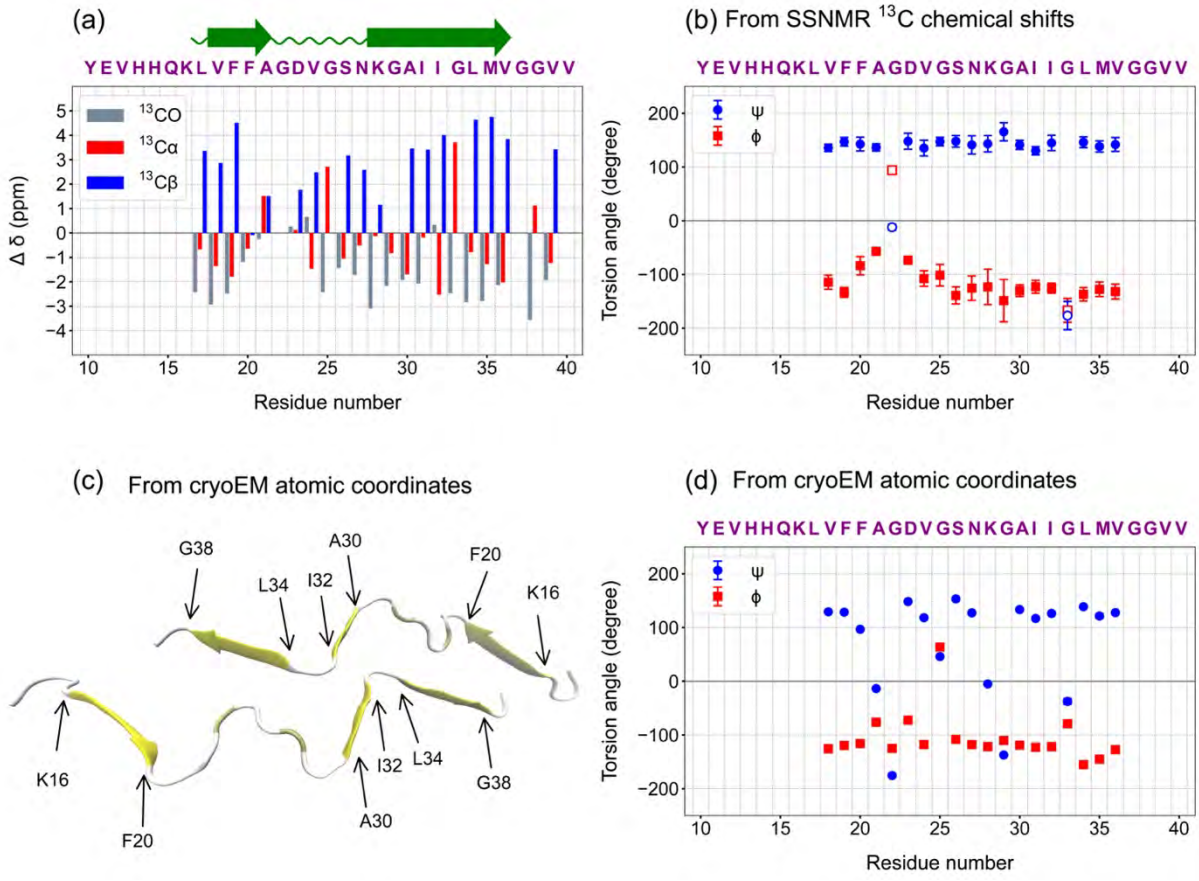

Supplementary Figure 14. (a) The secondary structure analysis by TALOS-N[9], showing 2 extended β-strand regions (green arrows) at the residues of V18–A21 and K28–V36 separated by loop/turn region (green wavy line) at the residues of G22–N27. (b) Dihedral angles (ϕ, ψ) calculated by TALOS-N[9] analysis, from ^{13}C chemical shifts (^{13}CO, $^{13}C_\alpha$, and $^{13}C_\beta$ from Supplementary Table 1) of quiescent seeded E22G Aβ40 fibril. Open markers at G22 and G33 designate the regions that were predicted with "warning". (c) Cartoon representation for the core layers of the model acquired by cryoEM for quiescent seeded E22G Aβ40 fibril, showing symmetry in β-strands from K16–F20 in both Aβ molecules but asymmetry from A30–G38. (d) Dihedral angles (ϕ, ψ) calculated from the atomic coordinates of Aβ molecules in the core layers of the proposed model in this work. Secondary structure analysis from SSNMR data in (b) was performed by TALOS-N.[9] The dihedral angles in (**d**) were extracted from the atomic coordinates using MDAnalysis[10,11].

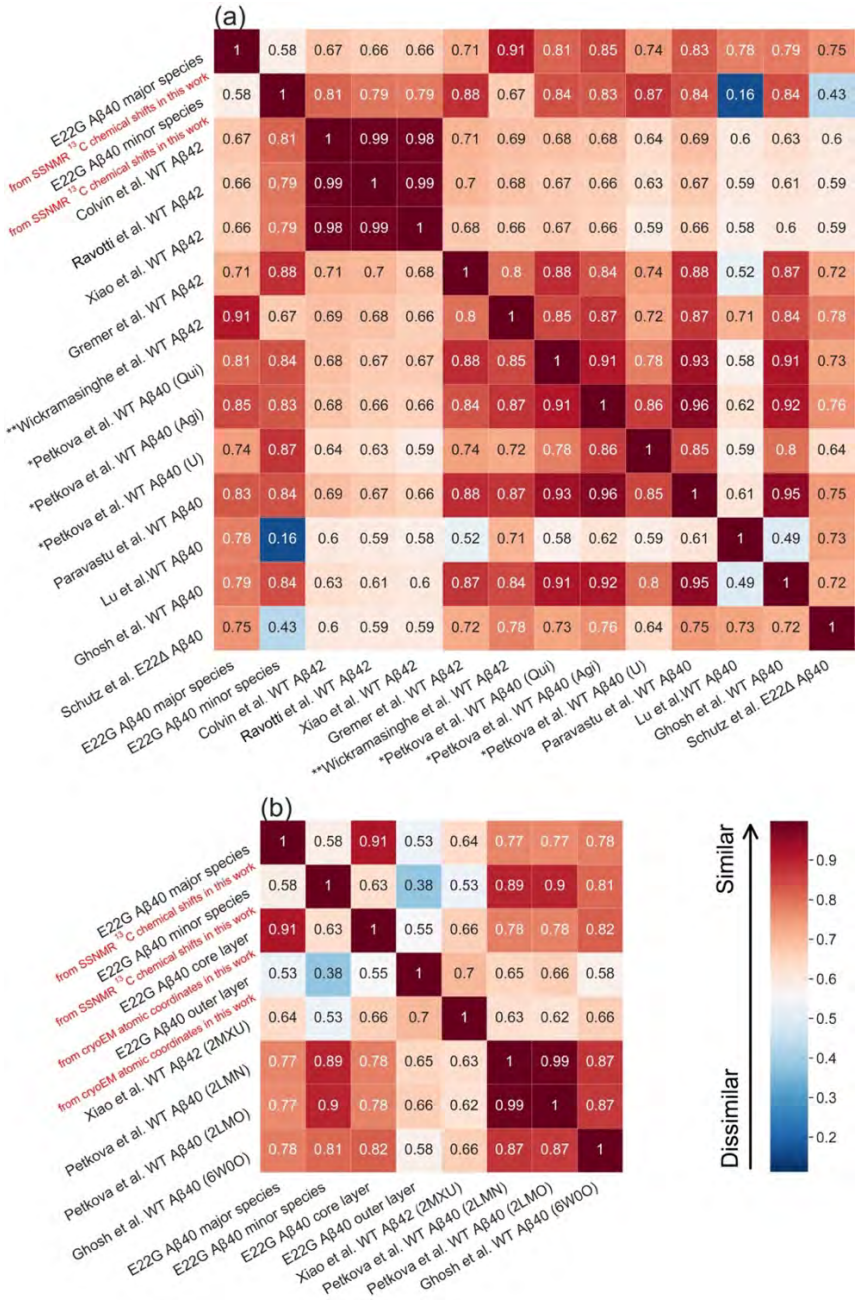

Supplementary Figure 15. (a) Heat map of Pearson's correlation coefficients (*r*) from experimental SSNMR ^{13}C secondary chemical shifts ($\Delta\delta$)[12] for ^{13}CO, $^{13}C_\alpha$, and $^{13}C_\beta$ of quiescent seeded E22G Aβ40 fibrils (from Supplementary Tables 1 and 2) compared with those of Aβ40[1,2,4,13-15] and Aβ42[5,16-19] fibrils previously reported in SSNMR structural studies, mapped out on a 14×14 matrix. (b) Heat map of *r* from experimental SSNMR ^{13}C secondary chemical shifts (^{13}CO, $^{13}C_\alpha$, and $^{13}C_\beta$) and from ShiftX2[20] calculated ^{13}C secondary chemical shifts from atomic coordinates of the quiescent seeded E22G Aβ40 fibrils obtained by cryoEM and ShiftX2 calculated ones from the atomic coordinates of some Aβ40[1,2,4] and Aβ42[5] fibril structures reported in the protein data bank (PDB) with the PDB identifiers, mapped out on an 8×8 matrix. *Qui: Quiescent, Agi: Agitated, and U: U-shaped. ^{13}C chemical shifts for Petkova (Qui) and (Agi) were reported for synthetic WT Aβ40 by Petkova *et al.*[13], and ** ^{13}C chemical shifts reported for recombinant WT Aβ42 in our lab by Wickramasinghe *et al.*[19], which may show high similarity to our model for E22G Aβ40 fibril presented in this work according to the obtained Pearson correlation coefficient.

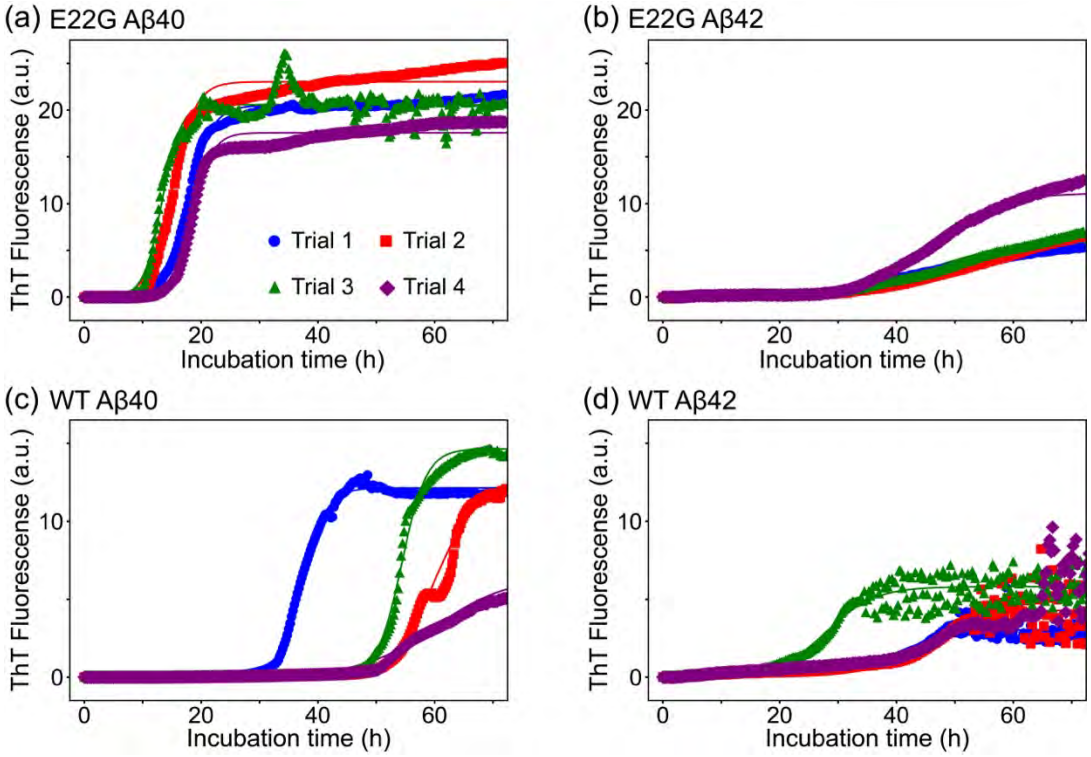

Supplementary Figure 16. Incubation time dependence of ThT fluorescence (in arbitrary unit, a.u.) for unseeded (a) E22G Aβ40, (b) E22G Aβ42, (c) WT Aβ40 and (d) WT Aβ42 prepared under quiescent conditions in a low salt phosphate buffer containing 0.02% NaN_3 and 5 mM NaCl. The monomer concentrations of Aβ are (a) 34, (b) 3, (c) 35, (d) 4 μM. The concentrations for (a–d) reflected the in-vivo concentration ratio of Aβ40/Aβ42 (i.e., ~10) in the Arctic FAD patients.[21] The fluorescence intensities were normalized by the Aβ concentrations for comparison. A comparison of the calculated average lag times is shown in Fig. 7a with the standard deviation values for the four trials.

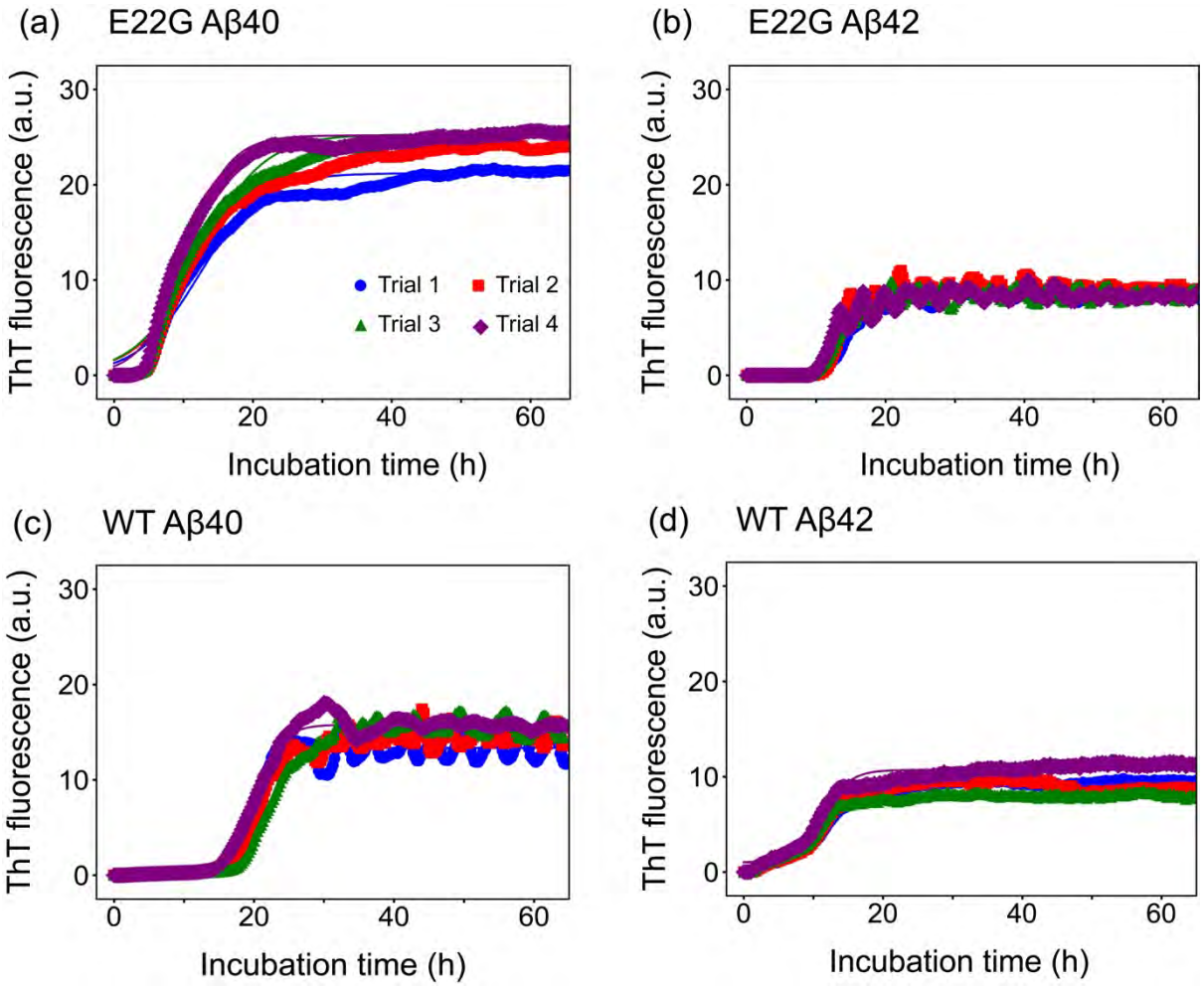

Supplementary Figure 17. Incubation time dependence of ThT fluorescence (in arbitrary unit, a.u.) for unseeded (a) E22G Aβ40, (b) E22G Aβ42, (c) WT Aβ40 and (d) WT Aβ42 prepared under quiescent conditions in a high salt condition mimicking an extracellular solution (20 mM HEPES, 140 mM NaCl, 5 mM KCl, 1 mM $MgSO_4$, 1 mM $CaCl_2$, 1 mM NaH_2PO_4, 5 mM D-(+)-glucose, 0.02% NaN_3, pH 7.5). The monomer concentrations of Aβ are (a) 15, (b) 1.6, (c) 16, and (d) 1.2 μM. The concentrations for (a–d) reflected in-vivo concentration ratio of Aβ40/Aβ42 (i.e., ~10) in the Arctic FAD patients.[21] The lag phase was reduced compared with that for Supplementary Fig. 16 due to the higher salt concentration of the extracellular buffer. However, the trends observed in Supplementary Fig. 16 were reproduced; that is, E22G Aβ40 self-assemble into fibril faster than other isoforms. The calculated average lag times were (a) 3.3 ± 0.4 h, (b) 10.6 ± 0.9 h, (c) 16.9 ± 0.8 h, and (d) 7.6 ± 0.8 h. The error range denotes the standard deviation of the four trials. The data in (a) suggest that in a situation similar to the physiological condition, E22G Aβ40 can self-assemble into fibril at a low μmol concentration within ~4 h. The fluorescence intensities were normalized by the Aβ concentrations for comparison.

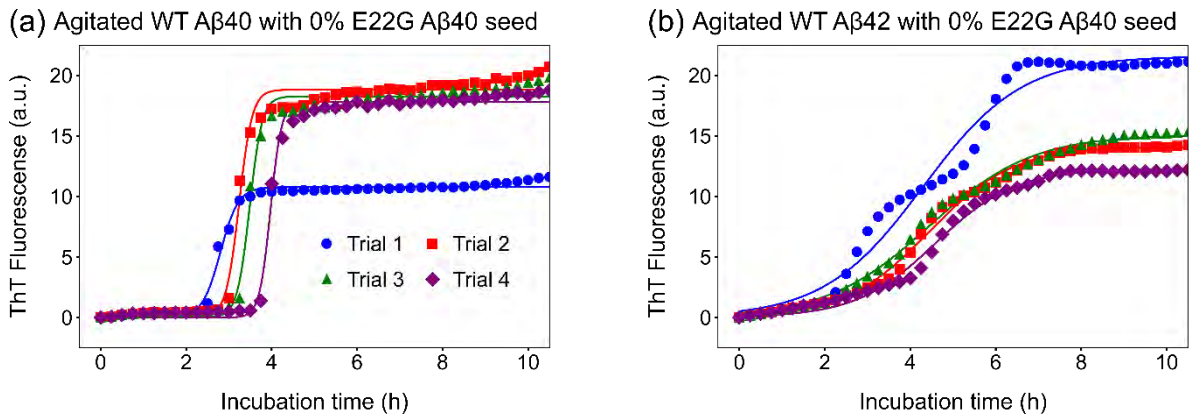

Supplementary Figure 18. Incubation time dependence of ThT fluorescence (in arbitrary unit, a.u.) for (a) WT Aβ40 and (b) WT Aβ42 in the absence of E22G Aβ40 fibril seed, prepared under agitated conditions in a low salt phosphate buffer containing 0.02% NaN_3 and 5 mM NaCl. The monomer concentrations of Aβ are (a) 42 and (b) 46 μM. The calculated average lag times were (a) 3.1 ± 0.5 h and (b) 2.3 ± 0.3 h. The error range denotes the standard deviation of the four trials. The fluorescence intensities were normalized by the Aβ concentrations for comparison.

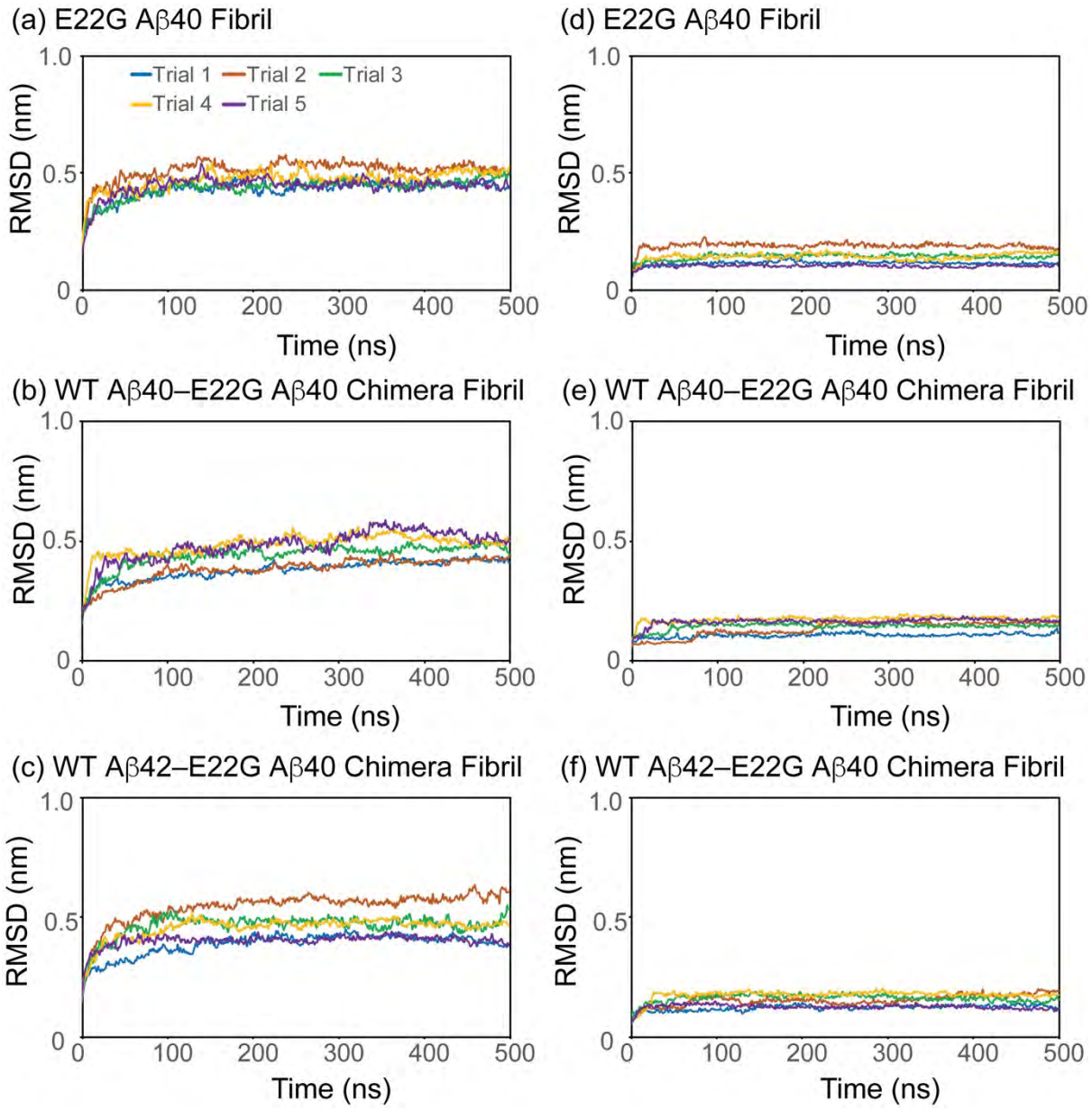

Supplementary Figure 19. The root-mean-squared deviation (RMSD) values of C_α positions in the MD simulation trajectories from the initial structure (the last frame extracted from the trajectory of stage 6) for (a, d) W-shaped fibril of E22G Aβ40, (b, e) W-shaped chimera fibril comprised of WT Aβ40 and E22G Aβ40, and (c, f) that of WT Aβ42 and E22G Aβ40 for (a–c) the entire system (residues 12–40) and (d–f) the stable central residues 22–36. For each structural model, five separate MD runs were performed. The RMSD values converged within 0.30−0.60 nm after ~200 ns for most trials. Relatively large RMSD values in (a–c) are attributed to the deviation of the β-sheet positions from the initial structure at the outer edge of the extended W-shape β-sheet core layers (see also Supplementary Figs. 20, 23), which are excluded from the calculations for (d–f). Representative MD structures at 500 ns for (a), (b), (c) are displayed in Fig. 7(d), (e), (f), respectively. The overlays of the structures from the five trails are shown in Supplementary Fig. 20(a–c).

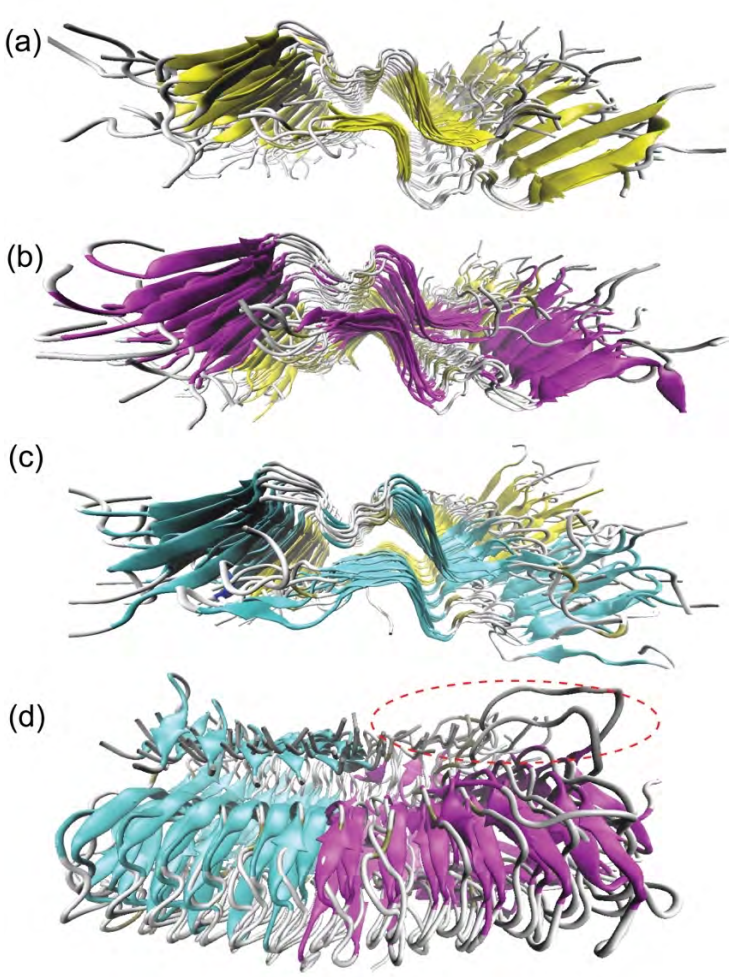

Supplementary Figure 20. Overlay of the MD structures at 500 ns from the five trails for (a) W-shaped fibril of E22G Aβ40 (yellow), (b) W-shaped chimera fibril comprised of WT Aβ40 (magenta) and E22G Aβ40 (yellow), (c) W-shaped chimera fibril comprised of WT Aβ42 (cyan) and E22G Aβ40 (yellow), and (d) S-shaped chimera fibril comprised of WT Aβ42 (cyan) and WT Aβ40 (magenta). With the omission of terminal Aβ molecules subject to the edge effects, (a–c) 16 Aβ and (d) 12 Aβ molecules are displayed for each structure. For the displayed 5 structures, the total RMSD values from the average structures for (a), (b), (c), and (d) were 2.41 Å, 2.69 Å, 2.80 Å, and 4.70 Å, respectively. The outer edge of the extended W-shaped β-sheets exhibits relatively large deviations among the five structures, suggesting the dynamic nature of the region. In contrast, the central region of the W-shaped β-sheets presents very similar structures. The results are consistent with the higher cryoEM resolution at the central region of the W-shaped β-sheet core layers and lower local resolution at the outer region (up to 3.8 Å; see Supplementary Fig. 8d). Despite the suggested dynamic nature, the W-shaped β-sheets are largely stable for all the models (see also Supplementary Fig. 21). Thus, the data in (b) and (c) for the chimera fibrils suggest the compatibility of WT Aβ40/Aβ42 and E22G Aβ40 in the cross-seeding for the W-shaped fibril structure. In contrast, for the S-shaped chimera fibril in (d), the β-sheets for the Aβ40 region are disrupted, for example, in the red dotted circled region, while the S-shaped β-sheet structures are retained in the Aβ42 side (see also Supplementary Fig. 22).

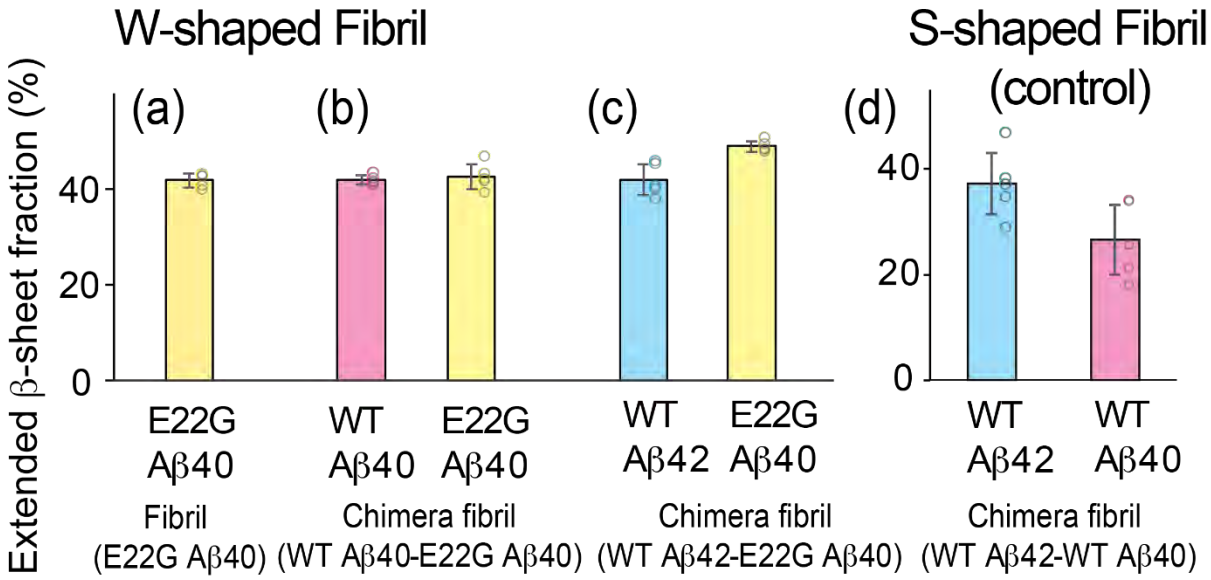

Supplementary Figure 21. The extended β-sheet fractions calculated from the MD simulation trajectories for (a) W-shaped fibril of E22G Aβ40 (yellow), (b) W-shaped chimera fibril comprised of WT Aβ40 (magenta) and E22G Aβ40 (yellow), (c) W-shaped chimera fibril comprised of WT Aβ42 (cyan) and E22G Aβ40 (yellow), and (d) S-shaped chimera fibril comprised of WT Aβ42 (cyan) and WT Aβ40 (magenta). The average β-sheet fraction values were calculated from the last 10 ns of the 500 ns simulations for 5 independent trials ($N = 5$) with each circle representing the value for each trial. The four Aβ molecules at the edge were excluded from the calculations. The error bars denote the standard deviations from the 5 trials. In (a)–(c), for the (a) W-shaped fibrils and (b, c) chimera fibrils, the β-sheet fractions are similar in a range of 42–49 %, demonstrating the stability of the chimera fibrils with both WT Aβ42 and WT Aβ40. In contrast, in (d) for the control data for the S-shaped chimera fibril, the β-sheet fraction for the WT Aβ40 (27 %) is substantially smaller than that for the WT Aβ42 (37 %) (see also Supplementary Fig. 22), which is consistent with the incompatibility of WT Aβ40 to the S-shaped WT Aβ42 fibril.

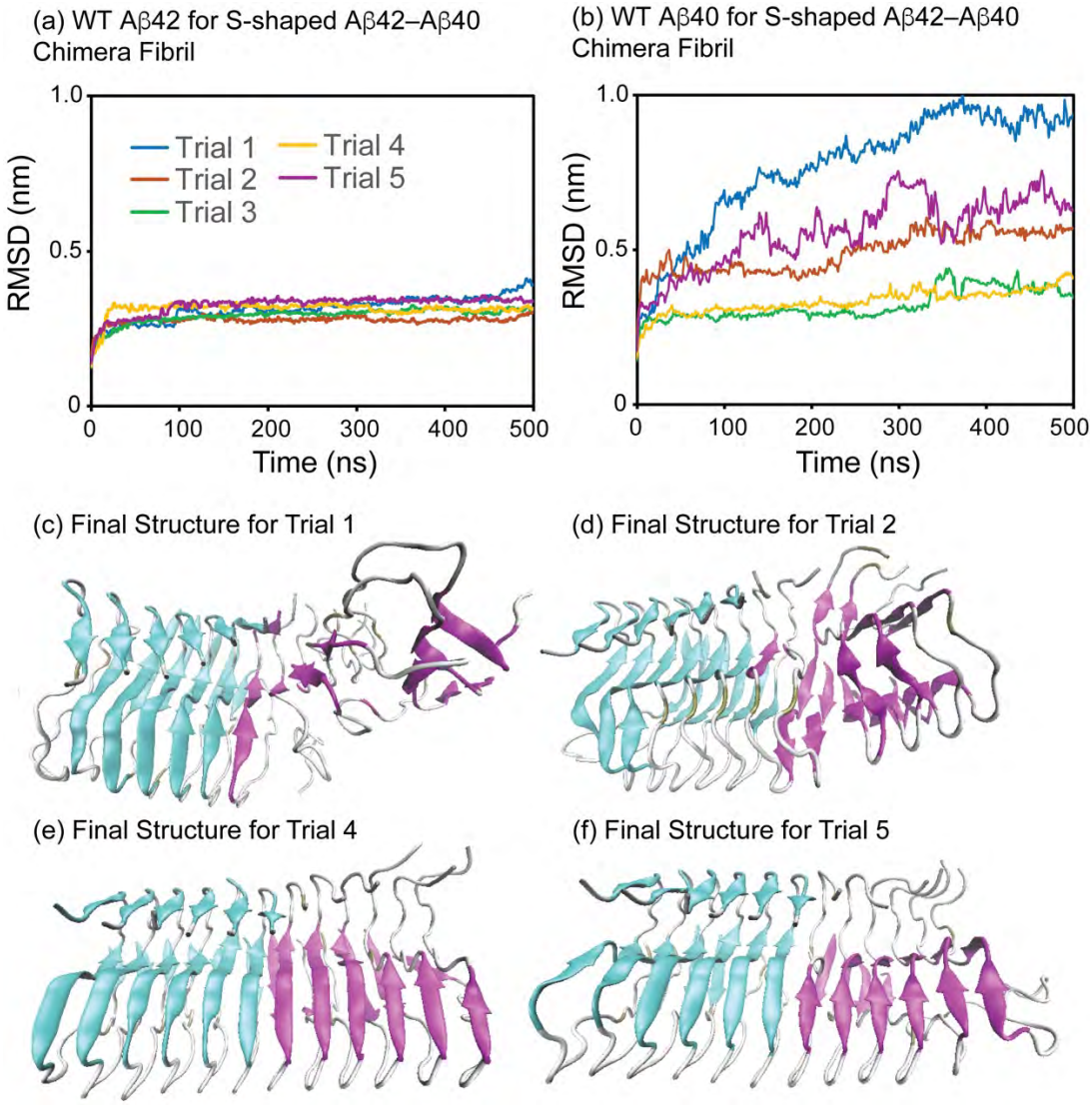

Supplementary Figure 22. (a, b) The root-mean-squared deviation (RMSD) values of C_α positions in the MD simulation trajectories for (a) the Aβ42 side and (b) Aβ40 side of the S-shaped chimera fibril comprised of WT Aβ42 and WT Aβ40. Five separate MD runs were performed, and the RMSD values were calculated from the initial structure (the last frame extracted from the trajectory of stage 6). The RMSD values converged within 0.31−0.41 nm after ~200 ns for most trials for the Aβ42 side in (a), while the RMSD values for the Aβ40 side exceeded 0.5 nm for the three trials (Trials 1, 2, 5) in (b). (c–f) MD structures at 500 ns for (c) Trial 1, (d) Trial 2, (e) Trial 4, (f) Trial 5. The cyan and magenta chains correspond to β sheets in Aβ42 and Aβ40 molecules, respectively. The corresponding structure for Trial 3 is shown in Fig. 7(g). For Trials 1 and 2, the β-sheets at the Aβ40 side were partially dissociated. The large RMSD values for the Aβ40 side in (b) are attributed to the partial dissociation of the β-sheets. The data also suggest that for all the trials, the S-shaped triple β-sheet structures are disrupted at the Aβ40 side.

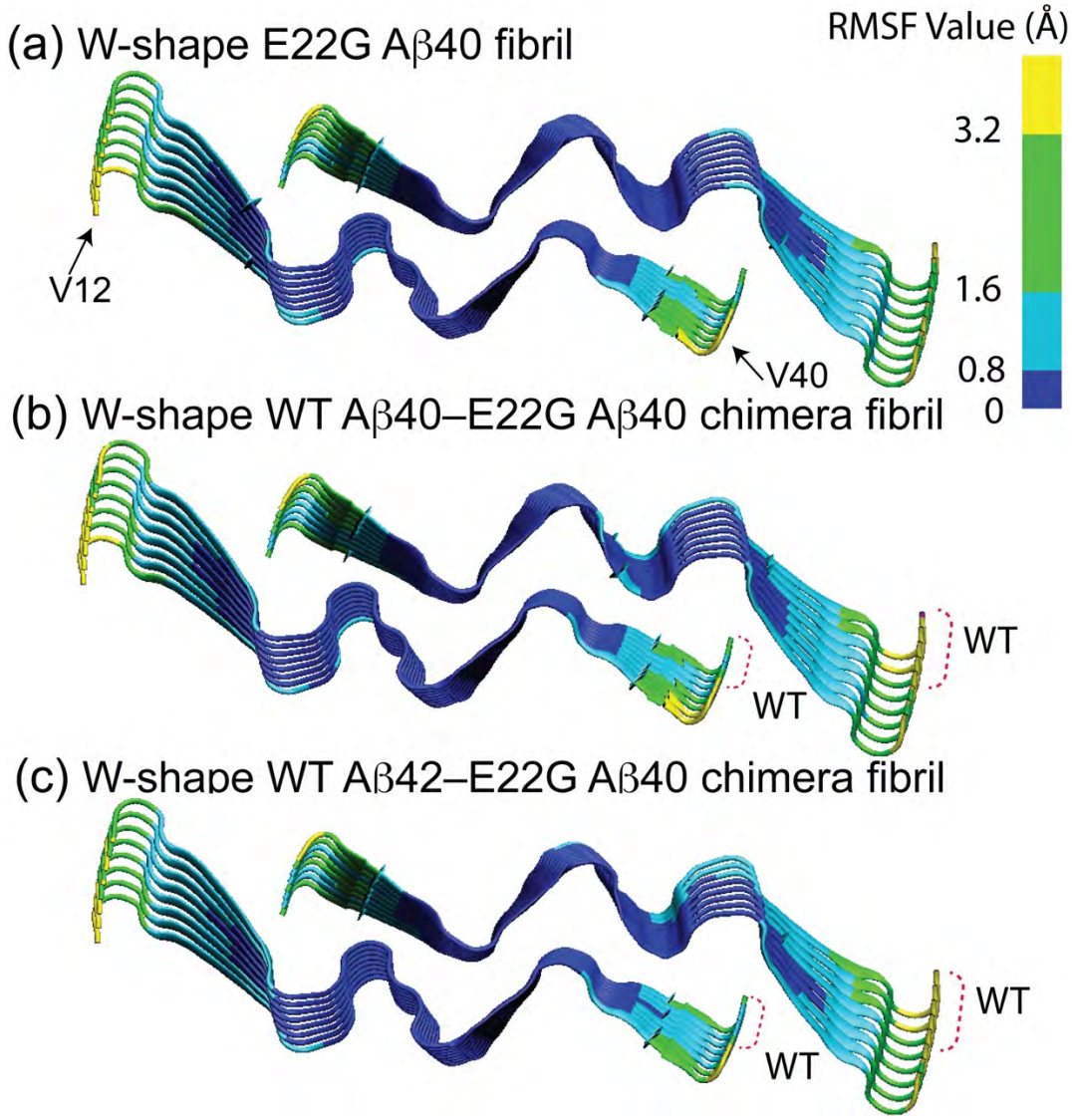

Supplementary Figure 23. Root-mean-square fluctuation (RMSF) values of C_α position mapped on the initial cryo-EM structure for the MD calculations of (a) W-shaped E22G Aβ40 fibril, (b) WT Aβ40- E22G Aβ40 chimera fibril, and (c) WT Aβ42- E22G Aβ40 chimera fibril. The relatively large fluctuations over 1.6 Å are restricted to the wing-like outer parts of the β-sheets in the W-shape fibrils for all the models. The data suggest the stability of the inner part of the W-shaped core layers, which is consistent with the cryoEM data. The data for the Aβ molecules at the edge of the fibrils were omitted. The chains at the back side of the figure correspond to the WT Aβ40 and Aβ42 in the chimera fibrils in (b) and (c), respectively.

Supplementary Tables

Supplementary Table 1. SSNMR ^{13}C chemical shifts of the major species of the quiescent seeded E22G Aβ40 fibril, referenced to DSS. The maximum error observed was 0.3 ppm.

Residue	^{13}CO	$^{13}C_{\alpha}$	$^{13}C_{\beta}$	$^{13}C_{\gamma1}$	$^{13}C_{\gamma2}$	$^{13}C_{\delta1}$	$^{13}C_{\delta2}$	$^{13}C_{\eta1}$	$^{13}C_{\eta2}$	$^{13}C_{\zeta}$
L17	174.5	54.2	45.4	28.1		27.6	25.7			
V18	173.0	61.0	34.6	22.5	21.2					
F19	173.1	55.9	43.7	138.7		131.3	131.3			
F20	174.5	57.2	39.1	139.1		132.4	132.4	130.9	130.9	127.4
A21	177.6	53.5	20.4							
D23	176.6	54.3	42.8	179.7						
V24	177.1	60.9	34.4	21.2	21.2					
G25	172.0	47.7								
S26	173.0	57.3	66.4							
N27	173.7	52.8	41.3	174.9						
K28	173.8	56.1	33.7	27.0		29.9		42.2		
G29	172.1	44.2								
A30	175.5	50.4	22.4							
I31	174.1	61.3	41.5	28.6	18.1	14.2				
I32	176.9	58.8	42.0	27.7	17.8	14.7				
G33	171.9	48.8								
L34	173.9	54.0	46.7	28.2		25.7	24.3			
M35	173.6	54.3	37.5	31.3				17.5		
V36	174.4	60.4	35.6	23.2	21.1					
G38	170.6	46.2								
V39	173.9	61.2	35.3	21.8	21.8					

Supplementary Table 2. SSNMR ^{13}C chemical shifts of the minor species of the quiescent seeded E22G Aβ40 fibril, referenced to DSS. The maximum error observed was 0.2 ppm.

Residue	^{13}CO	$^{13}C_\alpha$	$^{13}C_\beta$	$^{13}C_{\gamma1}$	$^{13}C_{\gamma2}$	$^{13}C_{\delta1}$	$^{13}C_{\delta2}$	$^{13}C_{\eta1}$	$^{13}C_{\eta2}$	$^{13}C_\zeta$
V18			36.2							
F20	173.0	55.8	43.4	139.1		132.5	132.5	131.3	131.3	
A21	175.2	50.4	22.3							
S26	173.4	55.3	65.4							
K28	174.4	56.1	35.0	27.1		30.1		42.5		
I32	174.5	60.1								
G33	170.6	44.7								
M35	176.2	54.7	36.5	32.9				18.1		

Supplementary Table 3. The relative SSNMR signal intensities of some resolved residues for the minor species of quiescent seeded E22G Aβ40 fibril sample with respect to those for the major species. The average value was obtained by arithmetic mean. The range of the error for the average value was obtained by $\sqrt{(\sum_{j=1}^{N} \varepsilon_j{}^2)/N}$, where N is the number of the relative intensity data (N =7) and ε_j represents the error for the j-th relative intensity value below.

Residue	Relative intensity (%)
F20	24 ± 13
A21	35 ± 6
S26	74 ± 7
K28	91 ± 21
I32	50 ± 12
G33	44 ± 3
M35	83 ± 12
Average	57 ± 5

Supplementary Table 4. Dihedral angles of quiescent seeded E22G Aβ40 fibril predicted by TALOS-N[9] from SSNMR data (^{13}CO, $^{13}C_\alpha$, and $^{13}C_\beta$ chemical shifts from Supplementary Table 1). The angles labeled with * were predicted with "Warning". The standard deviations were estimated from the TALOS-N software.[9]

Residue	ϕ	ψ
V18	-114.3 ± 13.1	135.7 ± 7.0
F19	-133.2 ± 9.2	146.9 ± 8.0
F20	-83.7 ± 17.0	142.6 ± 12.8
A21	-56.9 ± 5.4	136.5 ± 6.7
G22	94.0 ± 5.2*	-12.0 ± 5.7*
D23	-73.4 ± 7.2	148.0 ± 14.9
V24	-107.6 ± 14.3	135.2 ± 14.7
G25	-101.4 ± 19.9	147.3 ± 7.8
S26	-139.0 ± 15.9	147.9 ± 10.8

N27	-125.4 ± 22.7	141.2 ± 16.9
K28	-123.2 ± 32.9	143.3 ± 15.3
G29	-148.7 ± 39.4	165.6 ± 16.8
A30	-130.2 ± 10.8	141.2 ± 8.5
I31	-122.9 ± 11.8	130.4 ± 7.7
I32	-125.5 ± 9.2	144.9 ± 14.3
G33	-166.9 ± 22.2*	-176.6 ± 26.3*
L34	-136.8 ± 12.6	146.1 ± 10.0
M35	-127.6 ± 13.4	138.2 ± 10.4
V36	-131.9 ± 13.8	141.9 ± 12.8

Supplementary Table 5. Structural constraints from SSNMR data for quiescent seeded E22G Aβ40 fibril.

Type of constraint	Identified constraints	Number of constraints
Dihedral angles (ϕ,ψ)	V18-V36	19
Neighboring residues	F20-A21, A30-I31, G38-V39,	35
Long-range contacts from SSNMR	F20Cη-V24Cβ, F20Cζ-V24Cβ, F20Cγ-V24Cγ, F20Cδ-V24Cγ, F20Cη-V24Cγ, F20Cζ-V24Cγ, D23Cβ-S26Cβ, D23Cγ-S26Cα, D23Cγ-S26Cβ, D23C-S26Cβ, D23Cγ-K28Cδ, D23Cγ-K28Cη, D23C-K28Cδ, G25C-L34Cγ, G25C-L34Cδ2, G25Cα-V36Cγ1, G25Cα-V36Cγ2, G25C-V36Cγ1, G25C-V36Cγ2, N27Cα-I31Cα, N27Cα-I31Cγ1, N27Cα-I31Cγ2, N27Cα-I31Cδ, N27Cβ-L34Cβ, N27Cβ-L34Cδ1, I31Cα-G33Cα, I31Cα-G33C, I31Cβ-G33Cα, I31Cγ1-G33Cα, I31Cγ1-G33C, I31Cγ2-G33Cα, I31Cγ2-G33C, I31Cδ-G33Cα, I31Cδ-G33C, I32Cα-M35Cα, I32Cα-M35Cγ, I32Cβ-M35Cβ, I32Cβ-M35Cγ,	38
Missing contacts from SSNMR	L17-F20, L17-G25, L17-I32, L17-V36, V18-G25, V18-N27, V18-I31, V18-L34, F19-A30, F19-I31, F19-I32, F19-G33, F19-L34, F19-V36, F19-G38, F19-V39, F20-G25, F20-G29, F20-I31, F20-I32, F20-V36, A21-V24, A21-G29, A21-I31, D23-I32, D23-M35, V24-G29, V24-I31, G25-N27, G25-I31, G25-I32, S26-K28, S26-I32, S26-M35, K28-I32, K28-M35, G29-I31, A30-G33, A30-V36, I31-V36, I32-L34, I32-V36, I32-G38, I32-V39, G33-V36, L34-G38, L34-V39,	47

Supplementary Table 6. Parameters for cryoEM data collection, image processing, and molecular modeling for quiescent seeded E22G Aβ40 fibril.

Data Collection	
Microscope	Titan Krios
Voltage (kV)	300
Camera	K3-Summit
Magnification	105,000×
Defocus range (μm)	−0.5 to −2.5
Electron dose (e/Å)	50
Exposure time (s)	2.35
Pixel size (Å)	0.8285
Image Processing	
Box size (pix)	300
Inter-box distance (Å)	24.8
Number of extracted segments	478,295
Number of extracted segments after 2D classification	258,228
Number of extracted segments in final map	151,818
Resolution (FSC = 0.149)	2.5
Helical rise (Å)	4.77
Helical twist (°)	-2.17
Symmetry	*C*1
Molecular Modeling	
Non-hydrogen atoms	2080
Number of chains	10
Map CC (around atoms)	0.86
RMSD (bonds) (Å)	0.006
RMSD (angles) (°)	0.770
Clash score	3.55
Ramachandran outliers / favored (%)	0.00 / 88.89
Rotamer outliers (%)	10.95
C-beta deviations (%)	0.00
MolProbity score	2.51

Supplementary References

1. Ghosh, U., Thurber, K.R., Yau, W.-M. & Tycko, R. Molecular structure of a prevalent amyloid-β fibril polymorph from Alzheimer's disease brain tissue. *Proc. Natl. Acad. Sci. U. S. A.* **118**, e2023089118 (2021).
2. Petkova, A.T. et al. A structural model for Alzheimer's beta -amyloid fibrils based on experimental constraints from solid state NMR. *Proc. Natl. Acad. Sci. U. S. A.* **99**, 16742-7 (2002).
3. Petkova, A.T., Yau, W.-M. & Tycko, R. Experimental constraints on quaternary structure in Alzheimer's beta-amyloid fibrils. *Biochemistry* **45**, 498-512 (2006).

4. Paravastu, A.K., Leapman, R.D., Yau, W.-M. & Tycko, R. Molecular structural basis for polymorphism in Alzheimer's beta-amyloid fibrils. *Proc. Natl. Acad. Sci. U. S. A.* **105**, 18349-54 (2008).
5. Xiao, Y. et al. Aβ(1-42) fibril structure illuminates self-recognition and replication of amyloid in Alzheimer's disease. *Nat. Struct. Mol. Biol.* **22**, 499-505 (2015).
6. Yang, Y. et al. Cryo-EM structures of amyloid-β filaments with the Arctic mutation (E22G) from human and mouse brains. *Acta Neuropathologica*, **145**, 325-333 (2023).
7. Cock, P.J.A. et al. Biopython: freely available Python tools for computational molecular biology and bioinformatics. *Bioinformatics (Oxford, England)* **25**, 1422-3 (2009).
8. Nguyen, H., Case, D.A. & Rose, A.S. NGLview-interactive molecular graphics for Jupyter notebooks. *Bioinformatics (Oxford, England)* **34**, 1241-1242 (2018).
9. Shen, Y. & Bax, A. Protein backbone and sidechain torsion angles predicted from NMR chemical shifts using artificial neural networks. *J. Biomol. NMR* **56**, 227-41 (2013).
10. Michaud-Agrawal, N., Denning, E.J., Woolf, T.B. & Beckstein, O. MDAnalysis: a toolkit for the analysis of molecular dynamics simulations. *Journal of computational chemistry* **32**, 2319-27 (2011).
11. Gowers, R. et al. MDAnalysis: A Python Package for the Rapid Analysis of Molecular Dynamics Simulations. in *Proceedings of the 15th Python in Science Conference* 98-105 (2016).
12. Wishart, D.S., Bigam, C.G., Holm, A., Hodges, R.S. & Sykes, B.D. 1H, 13C and 15N random coil NMR chemical shifts of the common amino acids. I. Investigations of nearest-neighbor effects. *J. Biomol. NMR* **5**, 67-81 (1995).
13. Petkova, A.T. et al. Self-propagating, molecular-level polymorphism in Alzheimer's beta-amyloid fibrils. *Science (New York, N.Y.)* **307**, 262-5 (2005).
14. Lu, J.-X. et al. Molecular structure of β-amyloid fibrils in Alzheimer's disease brain tissue. *Cell* **154**, 1257-68 (2013).
15. Schütz, A.K. et al. Atomic-resolution three-dimensional structure of amyloid β fibrils bearing the Osaka mutation. *Angew. Chem.* **54**, 331-5 (2015).
16. Colvin, M.T. et al. High resolution structural characterization of Aβ42 amyloid fibrils by magic angle spinning NMR. *J. Am. Chem. Soc.* **137**, 7509-18 (2015).
17. Ravotti, F. et al. Solid-state NMR sequential assignment of an Amyloid-β(1-42) fibril polymorph. *Biomol. NMR assign.* **10**, 269-76 (2016).
18. Gremer, L. et al. Fibril structure of amyloid-β(1-42) by cryo-electron microscopy. *Science (New York, N.Y.)* **358**, 116-119 (2017).
19. Wickramasinghe, A. et al. Sensitivity-Enhanced Solid-State NMR Detection of Structural Differences and Unique Polymorphs in Pico- to Nanomolar Amounts of Brain-Derived and Synthetic 42-Residue Amyloid-β Fibrils. *J. Am. Chem. Soc.* **143**, 11462-11472 (2021).
20. Han, B., Liu, Y., Ginzinger, S.W. & Wishart, D.S. SHIFTX2: significantly improved protein chemical shift prediction. *J. Biomol. NMR* **50**, 43-57 (2011).
21. Nilsberth, C. et al. The 'Arctic' APP mutation (E693G) causes Alzheimer's disease by enhanced Abeta protofibril formation. *Nat. Neurosci.* **4**, 887-93 (2001).